Direct kinetic measurements and theoretical predictions of an isoprene-derived Criegee intermediate

Rebecca L. Caravan[a,b,c], Michael F. Vansco[d], Kendrew Au[b], M. Anwar H. Khan[e], Yu-Lin Li[f,g], Frank A. F. Winiberg[h,i], Kristen Zuraski[a], Yen-Hsiu Lin[f,g], Wen Chao[f], Nisalak Trongsiriwat[d], Patrick J. Walsh[d], David L. Osborn[b], Carl J. Percival[i], Jim Jr-Min Lin (林志民)[f,g], Dudley E. Shallcross[e], Leonid Sheps[b], Stephen J. Klippenstein[c], Craig A. Taatjes[b], and Marsha I. Lester[d,1]

[a]NASA Postdoctoral Program Fellow, NASA Jet Propulsion Laboratory, California Institute of Technology, Pasadena, CA 91109; [b]Combustion Research Facility, Sandia National Laboratories, Livermore, CA 94551; [c]Chemical Sciences and Engineering Division, Argonne National Laboratory, Lemont, IL 60439; [d]Department of Chemistry, University of Pennsylvania, Philadelphia, PA 19104-6323; [e]School of Chemistry, University of Bristol, Bristol BS8 1TS, United Kingdom; [f]Institute of Atomic and Molecular Sciences, Academia Sinica, Taipei 10617, Taiwan; [g]Department of Chemistry, National Taiwan University, Taipei 10617, Taiwan; [h]Division of Chemistry and Chemical Engineering, California Institute of Technology, Pasadena, CA 91125; and [i]NASA Jet Propulsion Laboratory, California Institute of Technology, Pasadena, CA 91109

Isoprene has the highest emission into Earth's atmosphere of any nonmethane hydrocarbon. Atmospheric processing of alkenes, including isoprene, via ozonolysis leads to the formation of zwitterionic reactive intermediates, known as Criegee intermediates (CIs). Direct studies have revealed that reactions involving simple CIs can significantly impact the tropospheric oxidizing capacity, enhance particulate formation, and degrade local air quality. Methyl vinyl ketone oxide (MVK-oxide) is a four-carbon, asymmetric, resonance-stabilized CI, produced with 21 to 23% yield from isoprene ozonolysis, yet its reactivity has not been directly studied. We present direct kinetic measurements of MVK-oxide reactions with key atmospheric species using absorption spectroscopy. Direct UV-Vis absorption spectra from two independent flow cell experiments overlap with the molecular beam UV-Vis-depletion spectra reported recently [M. F. Vansco, B. Marchetti, M. I. Lester, J. Chem. Phys. 149, 44309 (2018)] but suggest different conformer distributions under jet-cooled and thermal conditions. Comparison of the experimental lifetime herein with theory indicates only the *syn*-conformers are observed; *anti*-conformers are calculated to be removed much more rapidly via unimolecular decay. We observe experimentally and predict theoretically fast reaction of *syn*-MVK-oxide with SO_2 and formic acid, similar to smaller alkyl-substituted CIs, and by contrast, slow removal in the presence of water. We determine products through complementary multiplexed photoionization mass spectrometry, observing SO_3 and identifying organic hydroperoxide formation from reaction with SO_2 and formic acid, respectively. The tropospheric implications of these reactions are evaluated using a global chemistry and transport model.

atmospheric chemistry | Criegee intermediates | chemical kinetics | ab initio calculations | spectroscopy

Isoprene is a five-carbon, doubly unsaturated hydrocarbon with the highest emission into Earth's atmosphere of any nonmethane hydrocarbon. Its sources are predominantly biogenic, totaling 530 Tg per year (1), with abundances peaking between the tropics over the land mass where most of the Earth's biomass is located (e.g., the Amazon). An important sink of tropospheric isoprene [~10% (2)] is reaction with ozone, proceeding via 1,3-cycloaddition of ozone to either of the two C=C double bonds to give a primary ozonide (POZ). The POZ subsequently decomposes to form a carbonyl species and a carbonyl oxide, a zwitterionic reactive intermediate, known as a Criegee intermediate (CI) (3). Depending on the double bond to which ozone adds and how the POZ decomposes, four pairs of reaction products are possible: formaldehyde oxide (CH_2OO) + methyl vinyl ketone, formaldehyde oxide + methacrolein, methacrolein oxide

$[HC(OO)C(CH_2)CH_3]$ + formaldehyde, or methyl vinyl ketone oxide [MVK-oxide, $CH_3C(OO)CHCH_2$] + formaldehyde (Scheme 1). The resulting chemically activated CIs can undergo either rapid unimolecular decomposition or can be thermalized through collisions to form so-called stabilized CIs, that can subsequently undergo unimolecular and bimolecular reactions. Here we report direct measurements of unimolecular and bimolecular reactions of stabilized MVK-oxide at 298 K.

Global and local CI concentrations have previously been estimated via chemistry and transport models, using databases of alkene emissions (4). Concentration maxima are predicted in forested regions such as the Amazon, correlating with high isoprene emissions. With steady state CI concentrations $\leq 10^4$ cm^{-3} (4–8), two orders of magnitude lower than that of the principal tropospheric oxidant OH, reactivity of CIs with key pollutants

Significance

Ozonolysis is an important sink of alkenes in Earth's troposphere, leading to the formation of Criegee intermediates (CIs), whose reactions significantly impact tropospheric composition. The reactivity of the four-carbon unsaturated CIs derived from isoprene, the most abundant alkene, has remained unknown until now. Direct measurements of one such CI, methyl vinyl ketone oxide (MVK-oxide), with water vapor, SO_2, and formic acid are reported herein, substantiated by high-level theory, revealing the long lifetime of *syn*-MVK-oxide with respect to unimolecular decay and reaction with water vapor. Through a combination of direct experiment, high-level theory, and global modelling, *syn*-MVK-oxide is shown to survive high-humidity tropospheric environments and play a role in sulfuric acid formation and formic acid removal.

CHEMISTRY

Scheme 1. Reaction scheme illustrating the generation of MVK-oxide + formaldehyde from the ozonolysis of isoprene.

needs to be substantial to impact tropospheric lifetimes in comparison to OH-initiated processing. Low steady-state concentrations of CIs, resulting from slow production via ozonolysis and rapid subsequent decomposition, had until recently inhibited study of CI reactivity. Direct methods to photolytically generate simple CIs with carbon backbones containing up to three carbons (9–12) have enabled studies that revealed CI reactivity to be far greater than previously thought. Consequently, the flux of pollutant species, such as SO_2, through reaction with CIs could be significant.

The reaction of CH_2OO with the critical tropospheric pollutant SO_2 was shown to be 10,000 times faster than inferred from ozonolysis studies (11) and leads to the formation of SO_3, a critical sulfuric acid precursor in the troposphere that results in sulfate aerosol production (13–16). Subsequent chemistry and transport modeling suggests that tropospheric processing of SO_2 to SO_3 by CIs is comparable to SO_2 removal by OH in areas where CI concentrations are largest (4). CI + SO_2 reactions can account for as much as 46% of sulfuric acid production at ground level (15), increasing modeled particle nucleation rates by up to 820% (17) and, thus, impacting air quality, climate, and human health.

Reactions of CIs with organic acids have also been implicated in the formation of aerosols (18, 19). Fast removal of CIs by reaction with a number of organic acids has been measured (18–20). Global chemistry and transport modeling reveals that these reactions could significantly reduce modeled organic acid concentrations (18), with the greatest impacts over the Amazon area where CI concentrations are the highest (18). Through a combination of experimental and theoretical work for reactions of simple one- to three-carbon CIs, a mechanism has been identified whereby the CI undergoes a net insertion into the acid (18–20), leading to highly oxygenated, lower-volatility, functionalized organic hydroperoxides.

Due to the relatively high abundance of water in the troposphere, CI removal by reactions with water monomer and dimer can dominate over other reactive loss processes even for modest rate coefficients, constraining CI availability for other bimolecular reactions. However, through experimental work and theoretical studies, the rate coefficients for reactions of CIs with both water monomer and dimer have been shown to vary by orders of magnitude, depending on substituents and conformer of the CI. For example, a combination of experimental and theoretical studies of the two-carbon CI, acetaldehyde oxide, has shown that reactivity of the *syn-* and *anti-*conformers with water could differ by as much as five orders of magnitude (4, 10, 21–28). Therefore, the potential tropospheric impact of CIs is highly dependent on their structures.

MVK-oxide, a resonance-stabilized, four-carbon CI, is estimated to be produced from 21 to 23% of isoprene ozonolysis reactions under tropospheric conditions (2, 29). At present, local and global chemical models of the atmosphere represent the reactivity of four-carbon and higher, functionalized CIs based on direct measurements of the smaller H- or alkyl-substituted CIs. In MVK-oxide, the CI COO functional group is resonance stabilized with the vinyl side chain, potentially influencing reactivity and, thus, its role as a tropospheric oxidant. No direct measurements (22) have been performed on the reactions of resonance-stabilized CIs.

Like acetaldehyde oxide, MVK-oxide exists as distinct *syn-* and *anti-*conformers that do not interconvert at 298 K; *syn* and *anti* refer to the orientation of the terminal CI oxygen with respect to the methyl group of the carbon backbone. Each MVK-oxide conformer comprises two further configurations for the orientation of the vinyl group, *cis* and *trans*, that rapidly interconvert by rotation about the C–C bond at ~298 K (ref. 6 and *SI Appendix*). Until recently, no synthetic methods for the isolated production of MVK-oxide were known, preventing the direct study of the reactivity of either conformer. Barber et al. (30) recently reported a scheme for the selective production of MVK-oxide and employed this method to record an IR-action spectrum. The same scheme was used by Vansco et al. (31) to obtain a UV-Vis depletion spectrum, which displayed broad absorption features from 300 to 450 nm, consistent with both *syn-* and *anti-*conformers. Both studies generated MVK-oxide via 248 nm photolysis of 1,3-diiodobut-2-ene in O_2/Ar carrier gas that was sampled following supersonic expansion (T~10 K) under collision-free conditions. Vansco et al. (31) recorded the UV-Vis–induced depletion of the MVK-oxide photoionization signal (at 10.5 eV) on the mass-to-charge ratio (*m/z*) 86 (parent ion of
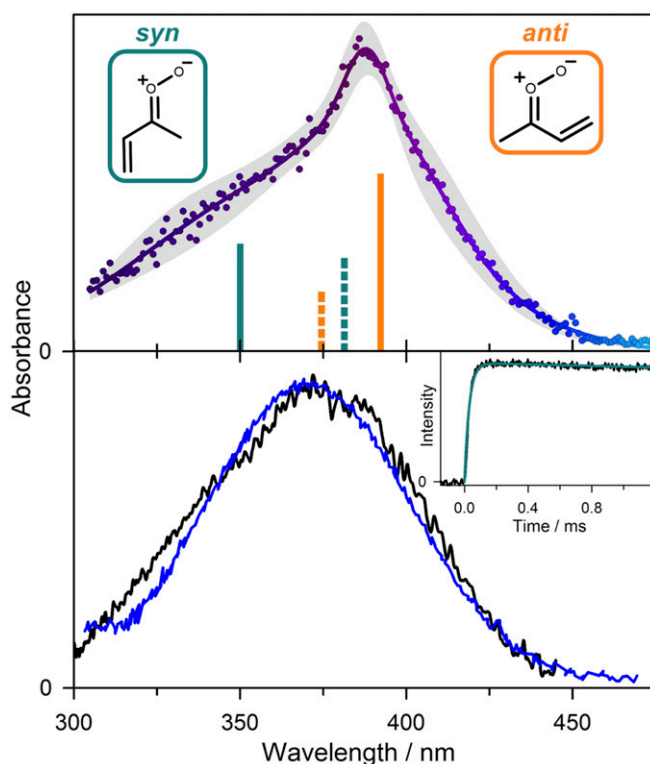

Fig. 1. (*Upper*) Electronic spectrum of MVK-oxide recorded under jet-cooled conditions by the UV-Vis induced depletion method from Vansco et al. (31). Data from ref. 31. (*Lower*) Direct absorption spectra obtained for MVK-oxide at 298 K using the Sandia broadband multipass transient absorption spectrometer (black) and IAMS absorption instrument (blue). Vertical excitation energies and associated oscillator strengths (bars, *Upper*) computed for the first $\pi^* \leftarrow \pi$ transition of MVK-oxide are shown for *syn-* (cyan) and *anti-* (orange) conformers; solid and dashed lines further distinguish between *trans* and *cis* configurations, respectively, which rapidly interconvert at 298 K. (*Lower Inset*) Kinetic time trace for MVK-oxide from the Sandia experiment (under 298 K, 10 Torr He; black) integrated between 330 and 367 nm compared with the simulated thermal unimolecular decay for *syn-*conformers to 2-hydroperoxyl-buta-1,3-diene (see Scheme 2) (cyan) with $k(T) = 33$ s^{-1}. Thermal rates are computed using ab initio master equation modeling in the high-pressure limit (30). The simulations include an experimental rise time for MVK-oxide appearance of 30 μs from the reaction of the iodoalkenyl radical with O_2 (*SI Appendix*).

MVK-oxide) mass channel. Additional studies indicated that MVK-oxide rapidly dissociates upon UV-Vis excitation to $O(^1D)$ products, providing evidence that the depletion measurements can be directly related to absorption.

For MVK-oxide, theory predicts relatively slow loss of both *syn-* and *anti-*conformers by reactions with water monomer and dimers, leading to first-order loss rates of ≤ 1 s^{-1} in the troposphere (6, 32). However, rapid unimolecular decay represents a potentially significant competitive loss process: thermal unimolecular loss rates at 298 K of 33 and 2,140 s^{-1} for *syn-* and *anti-*MVK-oxide conformers, respectively, have been calculated (30). Experimental observations to substantiate these unimolecular and water reaction loss rates, and to determine bimolecular reaction rate coefficients with key pollutant species, are therefore needed to evaluate the role of MVK-oxide in the troposphere.

The present study builds on the work of Vansco et al. (31) and reports direct absorption spectra of MVK-oxide at 298 K, obtained using two separate experiments (33–35). Using the characterized direct UV-Vis absorption spectra, we have employed broadband absorption spectroscopy to conduct direct bimolecular kinetics studies of MVK-oxide with key tropospheric species: SO_2, formic acid, and water. Complementary experiments using multiplexed photoionization mass spectrometry (MPIMS) and ab initio kinetic studies have been conducted to identify products resulting from reaction with SO_2 and formic acid and infer mechanisms. The implications of MVK-oxide reactivity on global sulfate aerosol formation and formic acid removal have been evaluated by a global three-dimensional chemistry and transport model, STOCHEM-CRI (stochastic chemistry and transport model with the common representative intermediates mechanism).

Results and Discussion

Spectroscopy and Unimolecular Decay.

MVK-oxide spectroscopy. The MVK-oxide electronic spectra recorded by direct absorption at 298 K using both the Sandia (34) and Institute of Atomic and Molecular Sciences (IAMS) (35) experimental apparatus span the same spectral range (300 to 450 nm) as that reported recently by Vansco et al. (31) using a depletion method under jet-cooled conditions (Fig. 1). The 298 K spectrum has a broad symmetric absorption from 300 to 450 nm, peaking at 370.6 nm with full width at half maximum (FWHM) of 73.4 nm (Gaussian fit to the IAMS spectrum). The electronic spectrum obtained by Vansco et al. (31) has a similarly broad but asymmetric profile peaked at 388 nm. We anticipate that the MVK-oxide conformer distribution may differ significantly at 298 K and under jet-cooled experimental conditions. We propose that this difference originates from the fast unimolecular decay of *anti-*conformers compared to *syn-*conformers at 298 K, discussed herein, and the rapid interconversion of *cis* and *trans* configurations.

The unimolecular decay mechanisms, transition state (TS) barriers, and thermal unimolecular decay rate coefficients for the *syn-* and *anti-*conformers of MVK-oxide differ considerably from one another. For *syn-*MVK-oxide conformers, unimolecular decay follows a 1,4 H-atom transfer mechanism that eventually releases OH radicals (Scheme 2). Thus, bimolecular reactions
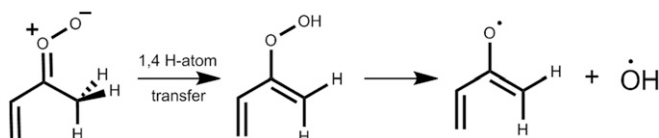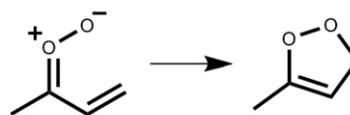
Scheme 3. Unimolecular isomerization of *anti-*MVK-oxide to the cyclic peroxide, dioxole, via 1,5 electrocyclic ring closure.

that compete with unimolecular decay in the troposphere will intercept OH production and may impact the oxidizing capacity of the troposphere.

The thermal decay rate for *syn-*MVK-oxide was experimentally benchmarked by the rate of appearance of OH products upon IR activation of *syn-*MVK-oxide, which agreed with an RRKM calculation based on an ab initio predicted TS barrier of 18.0 kcal mol^{-1} (30). Master equation calculations predicted a thermal unimolecular decay rate for *syn-*MVK-oxide of 33 s^{-1} (298 K, 1 atm, with ~10% reduction at 10 torr), which includes substantial contribution from H-atom tunneling. By contrast, theory predicts that *anti-*MVK-oxide conformers decay via a 1,5 electrocyclic ring closure process that forms a cyclic peroxide (Scheme 3), known as dioxole (6, 30, 36), with a TS barrier of only 12.0 kcal mol^{-1} and thermal decay rate of 2,140 s^{-1} (298 K, 1 atm) (30).

The transient absorption time trace for MVK-oxide obtained at 298 K in the Sandia experiment reveals a slow decay on the millisecond timescale as shown in Fig. 1 (*Lower Inset*; reproduced larger in *SI Appendix*). The experimental time profile agrees with a simulation using the predicted rate coefficient for *syn-*MVK-oxide of 33 s^{-1} (298 K), shown as a cyan line in Fig. 1, Inset (30, 36). Based on the theoretically predicted thermal decay rate coefficient for *anti-*MVK-oxide of 2,140 s^{-1} (298 K) (30), the time-resolved experiments should also exhibit a fast decay component, which is not observed. This suggests a faster decay rate possibly due to initial internal excitation of *anti-*MVK-oxide and/or low yield of the stabilized *anti-*conformer in the present 298 K experiments. This differs from prior studies under jet-cooled conditions with short delay times (20 µs) between

Scheme 2. Reaction mechanism for production of OH from *syn-*MVK oxide via 1,4 H-atom transfer to 2-hydroperoxybuta-1,3-diene.
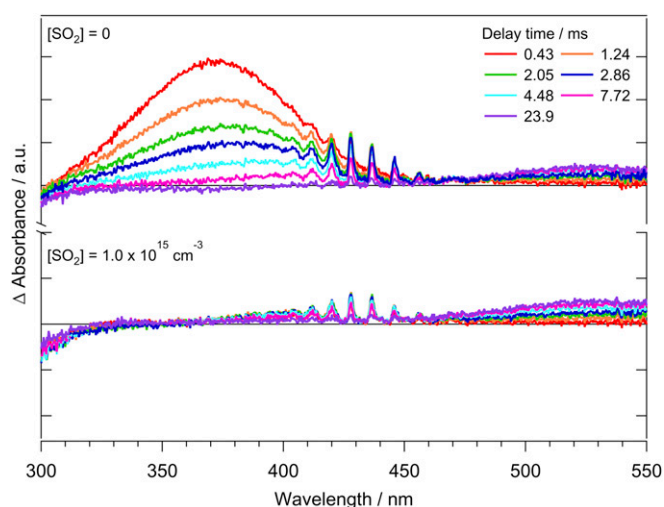
Fig. 2. Time-resolved difference absorption spectra recorded at 298 K and 7.4 Torr in the IAMS experiment resulting from (*Upper*) the photolysis of 1,3-diiodobut-2-ene in the presence of O_2 and (*Lower*) subsequent addition of $[SO_2] = 1.0 \times 10^{15}$ cm^{-3}. In addition to MVK-oxide, the transient spectra contain the spectral signatures of side products including IO and I_2 (see main text, *SO_2 scavenger experiments* section).

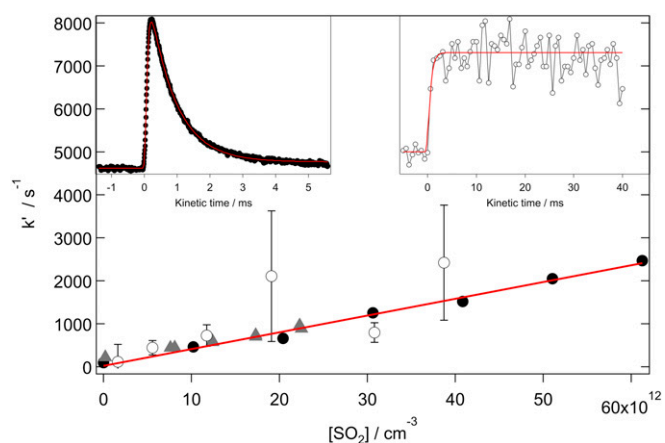**Fig. 3.** First-order rate coefficients for the reaction of *syn*-MVK-oxide with SO_2 as a function of $[SO_2]$, obtained from the decay of *syn*-MVK-oxide using the Sandia absorption experiment (black closed circles; 10 Torr total pressure with He bath gas, 95% confidence limit error bars), the IAMS absorption experiment (gray closed triangles; 4.1 Torr total pressure with O_2 bath gas, 340 nm probe wavelength, 95% confidence limit error bars), and SO_3 growth from the Sandia MPIMS experiment (open black circles; 10 Torr total pressure with He bath gas, 1σ error bars). Note that error bars for the black closed circles and gray closed triangles are smaller than the symbols. The red line is a linear fit to the Sandia absorption data, weighted by the 95% confidence limit error bars, obtaining a bimolecular rate coefficient of $(3.9 \pm 0.5) \times 10^{-11}$ cm^3 s^{-1}. (*Insets*) Typical time-resolved traces from the reaction of *syn*-MVK-oxide with SO_2: *syn*-MVK-oxide (Sandia absorption, 330 to 367 nm; *Top Left Inset*) and SO_3 (Sandia MPIMS, 13 eV ionization energy; *Top Right Inset*).

generation and probing, where spectroscopic features attributed to both *syn*- and *anti*-conformers of MVK-oxide were observed (31).

Comparison of the direct absorption and depletion measurements of the MVK-oxide electronic spectrum indicates that they match in the shorter-wavelength region, suggesting that *syn*-conformers likely dominate at $\lambda < 375$ nm in both experiments. At $\lambda > 375$ nm, a combination of *syn*- and *anti*-conformers appear to contribute to the jet-cooled spectrum, while predominantly *syn*-conformers give rise to the spectrum at 298 K. Theoretical calculations predict vertical transitions for the more stable *syn-trans* conformer at shorter wavelengths (350 nm) and *anti-trans* conformer at longer wavelengths (381 nm), although the computed electronic spectra (31) suggest they will be broad and overlapping. Rapid removal of *anti*-conformers at 298 K is consistent with the observed spectral changes and suggests that bimolecular reactions with the *anti*-conformer are unlikely to compete with unimolecular decay in the troposphere.

SO₂ scavenger experiments. Previous measurements of simple CIs have demonstrated rapid reaction with SO_2 (10, 11, 37, 38). To substantiate the assignment of the broad spectral feature to MVK-oxide, SO_2 was added to act as a scavenger for MVK-oxide in the IAMS experiments. Sufficient SO_2 was added to reduce the lifetime of MVK-oxide to <0.03 ms, assuming that the rate coefficient for MVK-oxide + SO_2 was comparable to that for $CH_2OO + SO_2$ (11, 38). Time-resolved spectra in the absence of SO_2 (Fig. 2, *Upper*) show the broad absorption feature assigned to MVK-oxide at 370 nm and its decay due to various experimental loss processes (e.g., wall loss and reactions with I atoms). The transient absorption spectra also show depletion signals at $\lambda < 320$ nm due to the precursor, structured features due to IO ($\lambda \sim 410$ to 450 nm) (39), and a broad feature from I_2 side-product ($\lambda \sim 450$ to 600 nm) (40). Note that even in the absence of SO_2, the decay in the IAMS experiment is more rapid than that

observed in the Sandia absorption experiment (Fig. 1, *Lower Inset*, and *SI Appendix*). In the latter, the experimental conditions were optimized to minimize bimolecular loss channels in order to observe unimolecular decay. In the presence of SO_2 (Fig. 2, *Lower*), the broad spectral feature centered at $\lambda \sim 370$ nm is absent, providing further evidence that this feature is due to MVK-oxide. Furthermore, the complete removal of this feature in <0.5 ms indicates that the bimolecular rate coefficient for MVK-oxide + SO_2 is rapid, as detailed below. By subtraction of the spectra in Fig. 2 (*Lower*) from those in Fig. 2 (*Upper*), the features due to MVK-oxide are obtained, as shown in Fig. 1. Note that this subtraction process does not perfectly remove spectral components due to IO, and so residual signal due to IO absorption at longer wavelengths has been manually removed to obtain the IAMS data presented in Fig. 1.

Bimolecular Kinetics. Using the direct UV-Vis absorption spectrum of *syn*-MVK-oxide, bimolecular kinetics with SO_2 and formic acid were investigated via broadband absorption spectroscopy. These experiments reveal that *syn*-MVK-oxide reactivity toward these species is similar to that of the smaller, H or alkyl-substituted CIs. Preliminary experiments also provide an upper limit for the very slow reaction of *syn*-MVK-oxide with water. The experimental observations are supported by high-level ab initio calculations that reveal much slower removal with water than for smaller CIs. Complementary investigations using MPIMS were undertaken to probe the products of the *syn*-MVK-oxide + SO_2 and formic acid reactions, and further mechanistic insight is provided through high level ab initio kinetics calculations. Additional MPIMS experiments were performed to obtain the formation kinetics of MVK-oxide from the reaction of the iodoalkenyl radical with O_2, the results of which are discussed in *SI Appendix*.

MVK-oxide + SO₂. Rapid removal of *syn*-MVK-oxide in the presence of SO_2 was observed from both the Sandia (10 Torr He/O_2) and IAMS (7 Torr N_2/O_2) experiments (Fig. 3). The pressure dependence of the *syn*-MVK-oxide + SO_2 rate coefficient across the total pressure range 4 to 700 Torr N_2 was investigated using
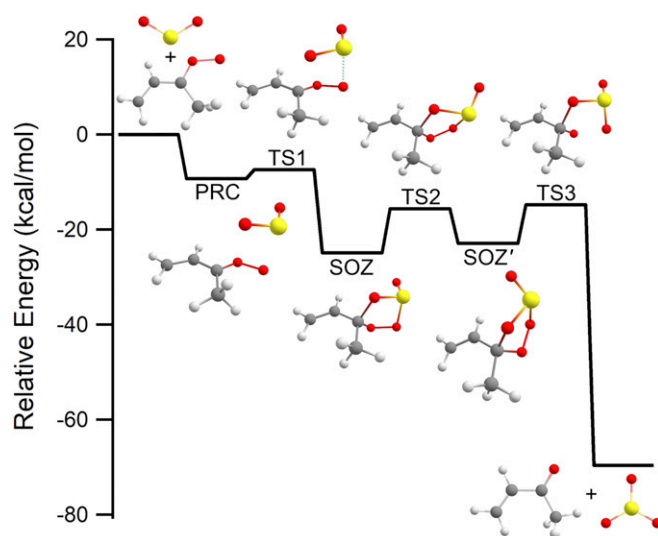

Fig. 4. Computed reaction coordinate of the *syn-trans;endo* path for the reaction *syn*-MVK-oxide with SO_2 at the CCSD(T)/CBS//B2PLYP-D3/cc-pVTZ level with estimated T(A) corrections (*SI Appendix*). The reaction proceeds through a prereactive complex (PRC) that forms secondary ozonides (SOZ and SOZ') via submerged barriers (TS1 and TS2). The SOZ subsequently decomposes in an exothermic reaction via TS3 to MVK + SO_3 products.
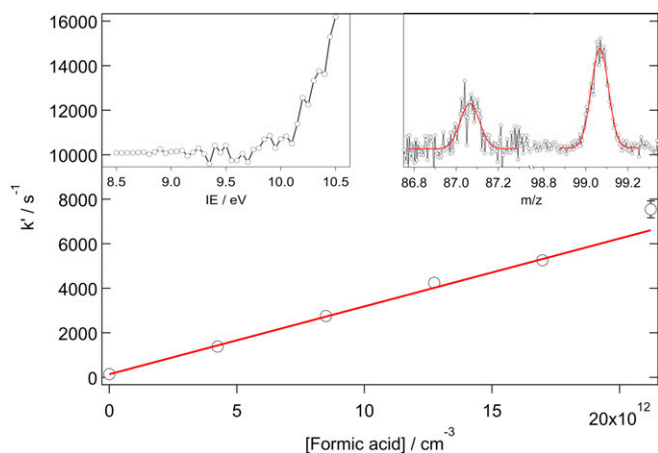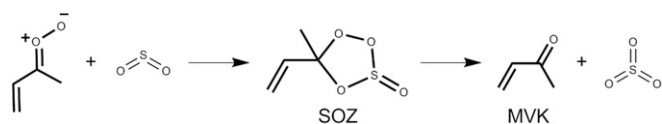
Fig. 5. First-order rate coefficients for the reaction of *syn*-MVK-oxide with formic acid as a function of formic acid concentration, obtained from the decay of *syn*-MVK-oxide using the Sandia absorption experiment. The red line is a linear fit to the absorption experiment data, weighted by the 95% confidence limit error bars, obtaining a bimolecular rate coefficient of $(3.0 \pm 0.1) \times 10^{-10}$ cm^3 s^{-1}. Note that some of the error bars are smaller than the symbols. (*Left Inset*) The photoionization spectrum for *m/z* 99 and (*Right Inset*) the mass spectrum of the proposed DI products, both obtained using MPIMS. Gaussian fits to the mass peaks yield exact masses of (87.042 ± 0.004) and (99.044 ± 0.001) amu, consistent with the exact masses of 87.045 (MVK-oxide + H, HCO$_2$-loss DI) and 99.045 (HO$_2$-loss DI) amu, respectively.

Scheme 4. Mechanism for the reaction of *syn*-MVK-oxide with SO$_2$, leading to the formation of methyl vinyl ketone + SO$_3$ via a secondary ozonide (SOZ).

the IAMS direct absorption experiment, and no significant dependence on pressure was observed. A rate coefficient of $(4.2 \pm 0.6) \times 10^{-11}$ cm^{3}s^{-1} (95% confidence limit error bar) at 298 K across the total pressure range 300 to 700 Torr N$_2$ is derived. This rate coefficient, supported by high-level computational kinetics calculations, is comparable with that reported for smaller CIs (4, 10, 11, 27, 33, 37, 38, 41, 42) and is consistent with effectively barrierless addition of MVK-oxide to SO$_2$, initially forming a secondary ozonide (SOZ) structure (Fig. 4 and Scheme 4). Ab initio calculations along the reaction coordinate reveal that the TS barrier(s) are comparatively higher for MVK-oxide + SO$_2$ vs. CH$_2$OO + SO$_2$ due to disruption of the extended conjugation of MVK-oxide. However, because the CH$_2$OO and MVK-oxide (Fig. 4) reactions proceed through strongly submerged barriers relative to the reactants, this results in minimal perturbation of the overall bimolecular rate coefficients.

Interrogation of the reaction products was undertaken through complementary MPIMS experiments at 10 Torr: SO$_3$ production was observed, with rise times consistent with CI loss kinetics, confirming SO$_3$ as a direct reaction product from *syn*-MVK-oxide + SO$_2$ (Fig. 3). Through rapid reaction of SO$_3$ with water in the troposphere, this reaction could represent a significant source of atmospheric sulfuric acid. Under the low-pressure conditions of these experiments, there was no substantive evidence for stabilized SOZ. To explore the pressure-dependent branching between SOZ stabilization and SO$_3$ + MVK formation, we implemented an ab initio TS theory-based master equation (AITSTME) model for the overall kinetic process. At 10 Torr, the AITSTME model demonstrates minimal stabilization of the SOZ (*SI Appendix*), supporting the experimental observations. Under tropospheric conditions, the higher density of states in the SOZ formed from larger CI reactions with SO$_2$ is predicted to result in increased SOZ lifetime (32), and third-body collisions are expected to form stabilized SOZ. At 300 K and 1 atm, ab initio kinetics calculations predict a ~5% yield of SOZ. However, the tropospheric fate of the SOZ remains uncertain with respect to decomposition or further reaction. The total rate coefficient is predicted to be effectively pressure-

independent, with no back reaction from the SOZ to the reactants. However, there is predicted to be a fairly strong temperature dependence due to the effect of the submerged barrier (TS1) connecting the prereactive complexes and the SOZ (*SI Appendix*).

MVK-oxide + formic acid. The kinetics of *syn*-MVK-oxide + formic acid were measured using the Sandia absorption experiment, yielding a rate coefficient of $(3.0 \pm 0.1) \times 10^{-10}$ cm^3 s^{-1} (Fig. 5). Reaction near the gas kinetic limit is consistent with the rapid reaction of smaller CIs with organic acids reported previously (18, 19). High-level ab initio calculations confirm the effectively barrierless net insertion of the CI into formic acid (Fig. 6 and Scheme 5), leading to a functionalized hydroperoxide, hydroperoxybut-3-en-2-yl formate (HPBF). However, the resonance stabilization in MVK-oxide significantly alters the potential energy surface of this reaction, compared to the CH$_2$OO case (43). For the CH$_2$OO reaction, Vereecken (43) found that the primary reaction pathway involves H transfer from the acid to the CI in concert with CO bond formation, followed by stabilization of the resulting functionalized hydroperoxide species. The functionalized hydroperoxide is much more weakly bound in the MVK-oxide reaction than in its CH$_2$OO analog [30 versus 44 kcal mol^{-1} (43)], due to the additional resonance stabilization present in MVK-oxide. In the CH$_2$OO case, stabilization of the adduct is predicted to dominate over bimolecular product formation, even though there is an exothermic exit channel arising from OO bond fission of the functionalized hydroperoxide. In the MVK-oxide case, the functionalized hydroperoxide is also favored over dissociation to produce OH + an alkoxy radical, which is now
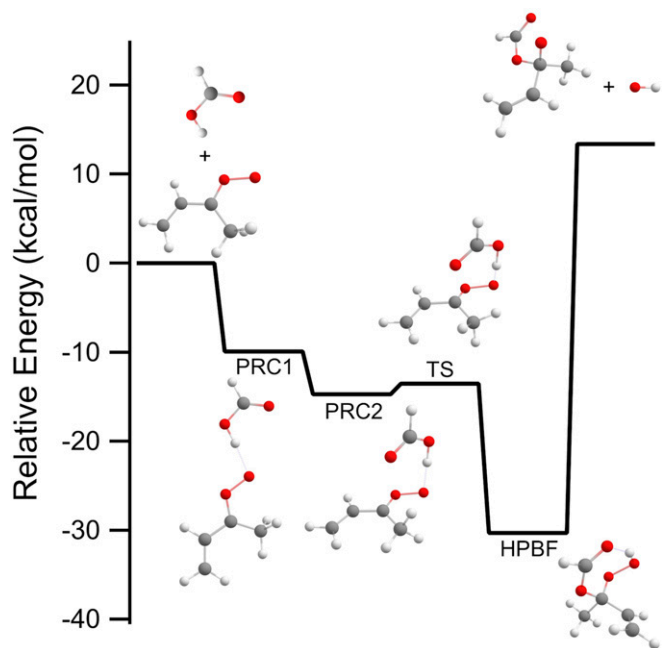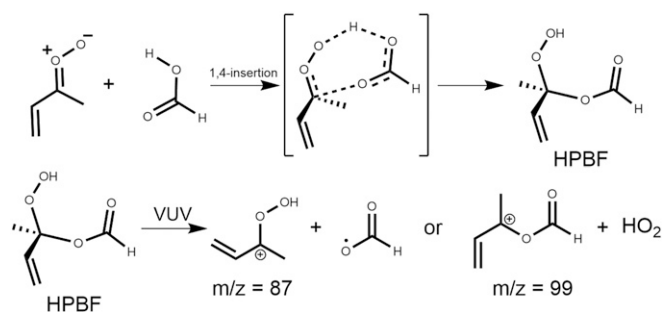

Fig. 6. Schematic plot of the reaction pathway for the addition of formic acid to *syn*-MVK-oxide. Stationary point energies are from CCSD(T)-F12/cc-pVTZ-F12//B2PLYPD3/cc-pVTZ calculations including zero-point energies.

Scheme 5. The 1,4-insertion of MVK-oxide into formic acid, leading to the formation of a functionalized hydroperoxide reaction product.

significantly endothermic relative to reactants. Despite these differences, the overall kinetics are predicted to be quite similar, with the reaction dominated by direct addition to form the functionalized hydroperoxide, HPBF, in the case of MVK-oxide (discussed in further detail in *SI Appendix*).

This reaction mechanism is supported by complementary MPIMS experiments that reveal the formation of species at exact masses corresponds to $C_4H_7O_2$ and $C_5H_7O_2$ (Fig. 5, *Top* and *Right Inset*). These products are consistent with characteristic HCO_2-loss (= protonated CI) and HO_2-loss daughter ions (DIs) from the dissociative photoionization of the predicted functionalized hydroperoxide reaction product, HPBF (18, 19, 44). The formation of the hydroperoxide product is further evidenced by the agreement between the observed and calculated vertical ionization energies and appearance energies for the m/z 99 DI (further details in *SI Appendix*).

Master equation-based predictions for the temperature and pressure dependencies of the *syn*-MVK-oxide + formic acid recombination rate coefficient are illustrated in Fig. 7. Notably, near room temperature, at pressures near 10 Torr (0.013 bar), the predicted rate coefficient is essentially identical to the experimentally observed value and strongly pressure-dependent. Although the present calculations were performed for N_2 as a

collider, the variation between N_2 and He should be quite modest. Importantly, at atmospheric pressure, the pressure dependence is greatly reduced with the rate coefficient effectively determined by the capture rate. At 1 bar, the predicted temperature dependence is well represented by the expression $7.7 \times 10^6\ T^{-5.86}\ \exp(-1{,}170/T)\ cm^3\ s^{-1}$ over the 200 to 400 K temperature region, with a predicted value of $4.9 \times 10^{-10}\ cm^3\ s^{-1}$ at room temperature.

MVK-oxide + water. Slow removal of *syn*-MVK-oxide in the presence of water vapor (where $[H_2O] \leq 5.7 \times 10^{17}\ cm^{-3}$, $[(H_2O)_2] \leq 7.9 \times 10^{14}\ cm^{-3}$) was observed experimentally, and upper limits of 4.0×10^{-17} and $3.0 \times 10^{-14}\ cm^3\ s^{-1}$ are derived from IAMS absorption experiments. These results are consistent with previous theoretical predictions of 9.5×10^{-20} and 9.0×10^{-17} $cm^3\ s^{-1}$ for the water monomer and dimer reaction rate coefficients (6, 45), respectively [or 8.1×10^{-20} and $3.1 \times 10^{-16}\ cm^3\ s^{-1}$, respectively, following adjustments made by Vereecken et al. (6) to account for the level of theory used; *SI Appendix*]. Higher-level kinetics calculations performed herein (see *SI Appendix* for further details) return a rate coefficient of $1.1 \times 10^{-19}\ cm^3\ s^{-1}$ for the *syn*-MVK-oxide + water monomer reaction, supporting the literature theoretical values (6, 45) and experimental upper limits reported here. By contrast, CH_2OO reacts rapidly with water and water dimer, with bimolecular rate coefficients of 2.4×10^{-16} and $6.6 \times 10^{-12}\ cm^3\ s^{-1}$, respectively, reported in the literature (46, 47), and thus, these reactions are a significant atmospheric sink of CH_2OO. We attribute the smaller reactivity of MVK-oxide vs. CH_2OO with water vapor to a higher TS barrier arising from disruption of the extended conjugation of *syn*-MVK-oxide in reaction leading to the hydroperoxide adduct. A prereactive complex exists for both reactions, and both have similar stabilities (-6.52 kcal mol^{-1} for CH_2OO vs. -6.11 kcal mol^{-1} for MVK-oxide). At the TS, the carbonyl oxide moiety begins bending out of plane, indicating that the extended conjugation is disrupted in the case of MVK-oxide. As a result, the TS barrier for the MVK-oxide + H_2O reaction is significantly higher (10.53 kcal mol^{-1} for MVK-oxide vs. 3.12 kcal mol^{-1} for CH_2OO), which dramatically lowers the reaction rate compared to $CH_2OO + H_2O$. Reaction with water will therefore not be an important sink of *syn*-MVK-oxide in the troposphere, and thus, MVK-oxide will survive high-humidity environments; this implies a relatively high tropospheric concentration of *syn*-MVK-oxide.

Atmospheric Modeling. The role of MVK-oxide in the troposphere has been evaluated through comparison of two model integrations, detailed herein. STOCHEM-CI0 represents our best current understanding of CI chemistry. It includes the reactions of MVK-oxide with SO_2, formic acid, water, and water dimer, in addition to unimolecular loss. STOCHEM-CI1 is a base-case scenario model wherein the reactions of MVK-oxide with SO_2 and formic acid are omitted (but still includes unimolecular decay and reactions with water and water dimer). In the model, *syn*- and *anti*-MVK-oxide are assumed to be produced from isoprene ozonolysis with yields of 0.14 and 0.07, respectively (29). The kinetic parameters utilized in both model integrations are detailed in *SI Appendix*.

Evaluation of STOCHEM-CI0 reveals that globally, MVK-oxide has the largest modeled steady-state concentration of all stabilized CIs (33% of the total CI molecules, 49% by weight). This is due to large isoprene emissions over forested regions and slow tropospheric removal through unimolecular decomposition and reactions with water and water dimer. If removal with SO_2 and formic acid are neglected (STOCHEM-CI1), the steady-state concentration of MVK-oxide increases slightly (36% of total CI molecules, 54% by weight). The slow removal via bimolecular reactions with water and water dimer and via unimolecular decomposition [33 s^{-1} at 298 K for *syn*-MVK-oxide (30) vs. ca. 300 s^{-1} for acetone oxide (37, 48, 49)] means that MVK-oxide
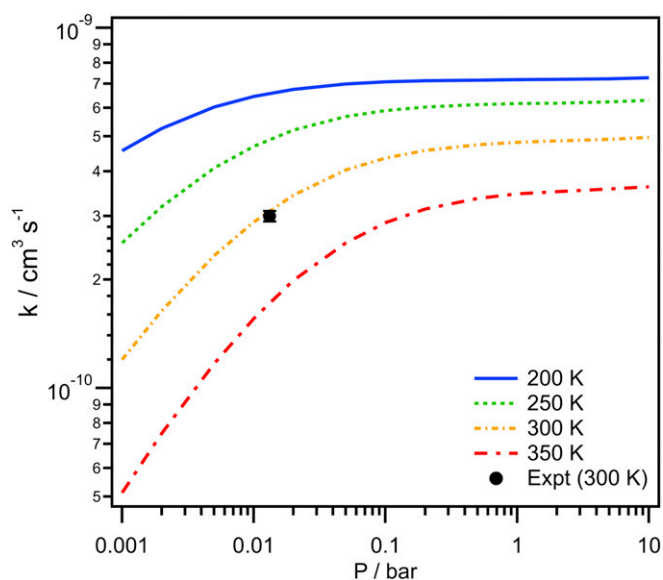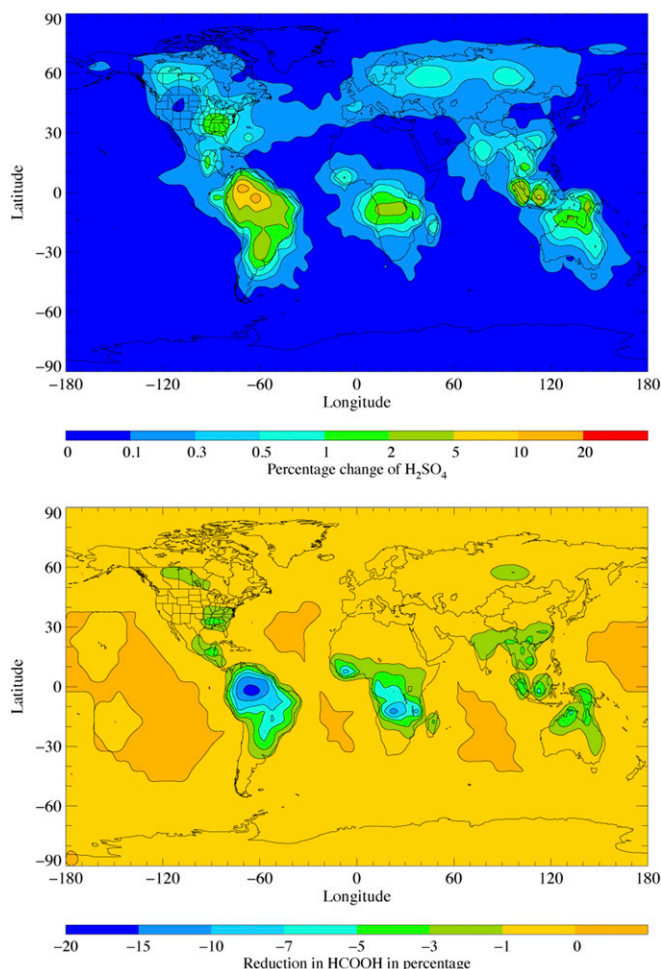

Fig. 7. Temperature and pressure dependencies of the *syn*-MVK-oxide + formic acid recombination rate coefficient computed based on ab initio TST-based master equation modeling. The experimental rate coefficient obtained in this work (solid black circle) is shown for comparison.

Fig. 8. Modeled implications of (*Upper*) MVK-oxide reaction with SO₂ on global sulfuric acid and (*Lower*) MVK-oxide reaction with formic acid on global formic acid evaluated using the global chemistry and transport model STOCHEM-CRI. Model evaluations presented result from comparison of our best current understanding of CI reactions (STOCHEM-CI0) with a case neglecting the contribution of MVK-oxide reactions with SO₂ and formic acid, but including unimolecular decomposition, reactions with water and water dimer, and unimolecular and bimolecular reactions of all other CIs (STOCHEM-CI1). Further details are given in *SI Appendix*.

will survive in high-humidity environments, and thus, other bimolecular reactions may be important.

We find that MVK-oxide plays a role in the tropospheric conversion of SO₂ to sulfuric acid (Fig. 8, *Upper*), the removal of formic acid (Fig. 8, *Lower*), and, potentially, particulate formation. Evaluation of STOCHEM-CI0 reveals that the reaction with SO₂ increases the SO₃ formation flux by 93% compared with the base-case scenario (STOCHEM-CI1), despite reaction with SO₂ accounting for only ∼2% of the total tropospheric loss of MVK-oxide. Previous modeling work has indicated that CIs are responsible for between 10 and 70% of all SO₂-initiated oxidation to sulfuric acid (15, 16, 50, 51). Neglecting the reaction of MVK-oxide + SO₂ leads to an 11% decrease in the tropospheric concentration of SO₃ globally, significantly impacting modeled sulfuric acid. For example, over the Amazon region, where isoprene emissions and subsequently MVK-oxide concentrations are highest, the reaction of MVK-oxide + SO₂ contributes up to 20% of sulfuric acid production. This source has modest implications for sulfate aerosol formation (*SI Appendix*).

The present work demonstrates that the reaction of the globally dominant and resonance stabilized CI, *syn*-MVK-oxide, with formic acid, is rapid. Evaluation of STOCHEM-CI0 reveals that reaction with MVK-oxide leads to up to 20% reduction in modeled formic acid globally (Fig. 8, *Lower*). Furthermore, the reactions of organic acids with CIs may contribute to the production of secondary organic aerosols via the formation of low-volatility, highly oxygenated products (19).

Conclusions

The direct UV-Vis absorption spectrum of the four-carbon, resonance-stabilized CI, MVK-oxide, has been recorded at 298 K in two independent experiments. We observe broad absorption centered around 370 nm in both experiments, in good agreement with the work of Vansco et al. (31), with differences attributed to the different conformer distribution in the 298 K and jet-cooled experiments. The different conformer distribution observed in the 298 K experiments suggests a low yield of stabilized *anti*-MVK-oxide and/or faster *anti*-MVK-oxide decomposition possibly due to internal excitation. The experimentally observed lifetime of MVK-oxide in the 298 K experiments is consistent with *syn*-conformers and substantiates rapid removal of *anti*-conformers as indicated by calculations of Barber et al. (6, 30).

Computation and direct experimental kinetic measurements of bimolecular reactions of *syn*-MVK-oxide demonstrate slow *syn*-MVK-oxide removal in the presence of water, confirming recent theoretical predictions (6, 45). Rapid reactivity with SO₂ and formic acid was observed and predicted theoretically, similar to C1 to C3 alkyl-substituted CIs (10, 11, 18, 19, 37). Complementary MPIMS measurements of the products from SO₂ and formic acid reactions with MVK-oxide indicate the potential role of these reactions in tropospheric particulate formation. SO₃ is observed from the reaction of *syn*-MVK-oxide with SO₂; global chemistry and transport modeling reveal a modest impact on predicted particle nucleation events due to the formation of sulfuric acid. The formation of a highly oxygenated organic hydroperoxide species, resulting from net insertion of the CI into the acid, was observed from the reaction of MVK-oxide with formic acid—recent chamber work has implicated similar species in the formation of secondary organic aerosols (52).

Methods and Materials

UV-Vis absorption spectra and bimolecular rate coefficients for MVK-oxide were recorded using two independent transient absorption experiments, both of which have been described in detail previously. Further details of both the Sandia and IAMS experiments are given in *SI Appendix*. Complementary experiments to identify the products of the MVK-oxide + SO₂ and formic acid reactions and to obtain the kinetics for MVK-oxide formation were undertaken using MPIMS, described previously and in *SI Appendix*. For all of the work reported herein, MVK-oxide was generated using the method of Barber et al. (30) using 1,3-diiodobut-2-ene photolysis in the presence of excess O₂. All experiments were performed under pseudo-first-order conditions, such that [O₂] >> [1,3-diiodobut-2-ene], and for bimolecular kinetics investigations, [co-reactant] >> [MVK-oxide]. Ab initio kinetics calculations were performed to supplement each of the experimental observations. They were based on a combination of density functional theory-based rovibrational analyses, coupled cluster-based energy evaluations, variational TS theory, and master equation analyses that explicitly treat hindered rotational motions. Further details are provided in *SI Appendix*. Modeling work was undertaken using STOCHEM-CRI which comprises a global chemistry transport model (STOCHEM) coupled with the common representative intermediate mechanism (CRI). This has been described previously and detailed further in *SI Appendix*.

Data Availability Statement. All data discussed in the paper are available in the main text and *SI Appendix*.

CHEMISTRY

1. C. Wiedinmyer, X. Tie, A. Guenther, R. Neilson, C. Granier, Future changes in biogenic isoprene emissions: How might they affect regional and global atmospheric chemistry? *Earth Interact.* **10**, 1–19 (2006).

2. T. B. Nguyen et al., Atmospheric fates of Criegee intermediates in the ozonolysis of isoprene. *Phys. Chem. Chem. Phys.* **18**, 10241–10254 (2016).

3. R. Criegee, Mechanism of ozonolysis. *Angew. Chem. Int. Ed. Engl.* **14**, 745–752 (1975).

4. M. A. H. Khan, C. J. Percival, R. L. Caravan, C. A. Taatjes, D. E. Shallcross, Criegee intermediates and their impacts on the troposphere. *Environ. Sci. Process. Impacts* **20**, 437–453 (2018).

5. A. Novelli et al., Estimating the atmospheric concentration of Criegee intermediates and their possible interference in a FAGE-LIF instrument. *Atmos. Chem. Phys.* **17**, 7807–7826 (2017).

6. L. Vereecken, A. Novelli, D. Taraborrelli, Unimolecular decay strongly limits the atmospheric impact of Criegee intermediates. *Phys. Chem. Chem. Phys.* **19**, 31599–31612 (2017).

7. M. A. H. Khan et al., An estimation of the levels of stabilized Criegee intermediates in the UK urban and rural atmosphere using the steady-state approximation and the potential effects of these intermediates on tropospheric oxidation cycles. *Int. J. Chem. Kinet.* **49**, 611–621 (2017).

8. R. Chhantyal-Pun et al., Direct kinetic and atmospheric modeling studies of Criegee intermediate reactions with acetone. *ACS Earth Space Chem.* **3**, 2363–2371 (2019).

9. C. A. Taatjes et al., Direct observation of the gas-phase Criegee intermediate (CH₂OO). *J. Am. Chem. Soc.* **130**, 11883–11885 (2008).

10. C. A. Taatjes et al., Direct measurements of conformer-dependent reactivity of the Criegee intermediate CH₃CHOO. *Science* **340**, 177–180 (2013).

11. O. Welz et al., Direct kinetic measurements of Criegee intermediate (CH₂OO) formed by reaction of CH₂I with O₂. *Science* **335**, 204–207 (2012).

12. F. Liu, J. M. Beames, A. M. Green, M. I. Lester, UV spectroscopic characterization of dimethyl- and ethyl-substituted carbonyl oxides. *J. Phys. Chem. A* **118**, 2298–2306 (2014).

13. R. A. Cox, S. A. Penkett, Aerosol formation from sulphur dioxide in the presence of ozone and olefinic hydrocarbons. *J. Chem. Soc. Faraday Trans.* **68**, 1735–1753 (1972).

14. R. A. Cox, S. A. Penkett, Oxidation of atmospheric SO₂ by products of the ozone-olefin reaction. *Nature* **230**, 321–322 (1971).

15. M. Boy et al., Oxidation of SO₂ by stabilized Criegee intermediate (sCI) radicals as a crucial source for atmospheric sulphuric acid concentrations. *Atmos. Chem. Phys.* **12**, 27693–27736 (2012).

16. R. L. Mauldin, 3rd et al., A new atmospherically relevant oxidant of sulfur dioxide. *Nature* **488**, 193–196 (2012).

17. C. J. Percival et al., Regional and global impacts of Criegee intermediates on atmospheric sulphuric acid concentrations and first steps of aerosol formation. *Faraday Discuss.* **165**, 45–73 (2013).

18. O. Welz et al., Rate coefficients of C(1) and C(2) criegee intermediate reactions with formic and acetic acid near the collision limit: Direct kinetics measurements and atmospheric implications. *Angew. Chem. Int. Ed. Engl.* **53**, 4547–4550 (2014).

19. R. Chhantyal-Pun et al., Criegee intermediate reactions with carboxylic acids: A potential source of secondary organic aerosol in the atmosphere. *ACS Earth Space Chem.* **2**, 833–842 (2018).

20. C. A. Taatjes et al., Reaction of perfluorooctanoic acid with Criegee intermediates and implications for the atmospheric fate of perfluorocarboxylic acids. *Environ. Sci. Technol.* **53**, 1245–1251 (2019).

21. B. Long, J. L. Bao, D. G. Truhlar, Atmospheric chemistry of Criegee intermediates: Unimolecular reactions and reactions with water. *J. Am. Chem. Soc.* **138**, 14409–14422 (2016).

22. M. J. Newland et al., Atmospheric isoprene ozonolysis: Impacts of stabilised Criegee intermediate reactions with SO₂, H₂O and dimethyl sulfide. *Atmos. Chem. Phys.* **15**, 9521–9536 (2015).

23. L.-C. Lin et al., Competition between H₂O and (H₂O)₂ reactions with CH₂OO/CH₃CHOO. *Phys. Chem. Chem. Phys.* **18**, 4557–4568 (2016).

24. J. M. Anglada, J. González, M. Torrent-Sucarrat, Effects of the substituents on the reactivity of carbonyl oxides. A theoretical study on the reaction of substituted carbonyl oxides with water. *Phys. Chem. Chem. Phys.* **13**, 13034–13045 (2011).

25. J. M. Anglada, P. Aplincourt, J. M. Bofill, D. Cremer, Atmospheric formation of OH radicals and H₂O₂ from alkene ozonolysis under humid conditions. *ChemPhysChem* **3**, 215–221 (2002).

26. A. B. Ryzhkov, P. A. Ariya, A theoretical study of the reactions of parent and substituted Criegee intermediates with water and the water dimer. *Phys. Chem. Chem. Phys.* **6**, 5042–5050 (2004).

27. L. Sheps, A. M. Scully, K. Au, UV absorption probing of the conformer-dependent reactivity of a Criegee intermediate CH₃CHOO. *Phys. Chem. Chem. Phys.* **16**, 26701–26706 (2014).

28. L.-C. Lin, W. Chao, C.-H. Chang, K. Takahashi, J. J. Lin, Temperature dependence of the reaction of anti-CH₃CHOO with water vapor. *Phys. Chem. Chem. Phys.* **18**, 28189–28197 (2016).

29. D. Zhang, W. Lei, R. Zhang, Mechanism of OH formation from ozonolysis of isoprene: Kinetics and product yields. *Chem. Phys. Lett.* **358**, 171–179 (2002).

30. V. P. Barber et al., Four-carbon Criegee intermediate from isoprene ozonolysis: Methyl vinyl ketone oxide synthesis, infrared spectrum, and OH production. *J. Am. Chem. Soc.* **140**, 10866–10880 (2018).

31. M. F. Vansco, B. Marchetti, M. I. Lester, Electronic spectroscopy of methyl vinyl ketone oxide: A four-carbon unsaturated Criegee intermediate from isoprene ozonolysis. *J. Chem. Phys.* **149**, 244309 (2018).

32. L. Vereecken, H. Harder, A. Novelli, The reaction of Criegee intermediates with NO, RO₂, and SO₂, and their fate in the atmosphere. *Phys. Chem. Chem. Phys.* **14**, 14682–14695 (2012).

33. L. Sheps, Absolute ultraviolet absorption spectrum of a Criegee intermediate CH₂OO. *J. Phys. Chem. Lett.* **4**, 4201–4205 (2013).

34. L. Sheps, D. W. Chandler, *Time-Resolved Broadband Cavity-Enhanced Absorption Spectroscopy for Chemical Kinetics* (Sandia National Laboratories SNL-CA, Livermore, CA, 2013).

35. M.-N. Su, J. J.-M. Lin, Note: A transient absorption spectrometer using an ultra bright laser-driven light source. *Rev. Sci. Instrum.* **84**, 086106 (2013).

36. K. T. Kuwata, L. C. Valin, A. D. Converse, Quantum chemical and master equation studies of the methyl vinyl carbonyl oxides formed in isoprene ozonolysis. *J. Phys. Chem. A* **109**, 10710–10725 (2005).

37. R. Chhantyal-Pun et al., Direct measurements of unimolecular and bimolecular reaction kinetics of the Criegee intermediate (CH₃)₂COO. *J. Phys. Chem. A* **121**, 4–15 (2017).

38. D. Stone, M. Blitz, L. Daubney, N. U. Howes, P. Seakins, Kinetics of CH₂OO reactions with SO₂, NO₂, NO, H₂O and CH₃CHO as a function of pressure. *Phys. Chem. Chem. Phys.* **16**, 1139–1149 (2014).

39. P. Spietz, J. C. G. Martín, J. P. Burrows, Spectroscopic studies of the I₂/O₃ photochemistry: Part 2. Improved spectra of iodine oxides and analysis of the IO absorption spectrum. *J. Photochem. Photobiol. Chem.* **176**, 50–67 (2005).

40. J. Burkholder et al., *Chemical Kinetics and Photochemical Data for Use in Atmospheric Studies* (Eval. 18, Jet Propulsion Laboratory, Pasadena, 2015), vol. 15–10.

41. Y. Liu et al., A kinetic study of the CH₂OO Criegee intermediate reaction with SO₂, (H₂O)₂, CH₂I₂ and I atoms using OH laser induced fluorescence. *Phys. Chem. Chem. Phys.* **19**, 20786–20794 (2017).

42. H.-L. Huang, W. Chao, J. J.-M. Lin, Kinetics of a Criegee intermediate that would survive high humidity and may oxidize atmospheric SO₂. *Proc. Natl. Acad. Sci. U.S.A.* **112**, 10857–10862 (2015).

43. L. Vereecken, The reaction of Criegee intermediates with acids and enols. *Phys. Chem. Chem. Phys.* **19**, 28630–28640 (2017).

44. R. Chhantyal-Pun et al., Experimental and computational studies of Criegee intermediate reactions with NH₃ and CH₃NH₂. *Phys. Chem. Chem. Phys.* **21**, 14042–14052 (2019).

45. J. M. Anglada, A. Solé, Impact of the water dimer on the atmospheric reactivity of carbonyl oxides. *Phys. Chem. Chem. Phys.* **18**, 17698–17712 (2016).

46. L. Sheps et al., The reaction of Criegee intermediate CH₂OO with water dimer: Primary products and atmospheric impact. *Phys. Chem. Chem. Phys.* **19**, 21970–21979 (2017).

47. W. Chao, J.-T. Hsieh, C.-H. Chang, J. J.-M. Lin, Direct kinetic measurement of the reaction of the simplest Criegee intermediate with water vapor. *Science* **347**, 751–754 (2015).

48. Y. Fang, V. P. Barber, S. J. Klippenstein, A. B. McCoy, M. I. Lester, Tunneling effects in the unimolecular decay of (CH₃)₂COO Criegee intermediates to OH radical products. *J. Chem. Phys.* **146**, 134307 (2017).

49. M. C. Smith, W. Chao, K. Takahashi, K. A. Boering, J. J.-M. Lin, Unimolecular decomposition rate of the Criegee intermediate (CH₃)₂COO measured directly with UV absorption spectroscopy. *J. Phys. Chem. A* **120**, 4789–4798 (2016).

50. G. Sarwar et al., Impact of sulfur dioxide oxidation by Stabilized Criegee Intermediate on sulfate. *Atmos. Environ.* **85**, 204–214 (2014).

51. J. Li, Q. Ying, B. Yi, P. Yang, Role of stabilized Criegee intermediates in the formation of atmospheric sulfate in eastern United States. *Atmos. Environ.* **79**, 442–447 (2013).

52. Y. Sakamoto, S. Inomata, J. Hirokawa, Oligomerization reaction of the Criegee intermediate leads to secondary organic aerosol formation in ethylene ozonolysis. *J. Phys. Chem. A* **117**, 12912–12921 (2013).